Int. J. Heat Mass Transfer. Vol. 30, No. 2, pp. 251–262, 1987
Printed in Great Britain

0017-9310/87 $3.00 + 0.00
Pergamon Journals Ltd.

A three-dimensional analysis of natural convection in a toroidal loop—the effect of Grashof number

ADRIENNE S. LAVINE,† RALPH GREIF‡ and JOSEPH A. C. HUMPHREY‡

† Mechanical, Aerospace and Nuclear Engineering Department, University of California—Los Angeles, Los Angeles, CA 90024, U.S.A.

‡ Department of Mechanical Engineering, University of California Berkeley, Berkeley, CA 94720, U.S.A.

(*Received* 12 *September* 1985 *and in final form* 15 *May* 1986)

Abstract—A three-dimensional, numerical analysis of natural convection in a closed, toroidal loop has been performed. The results show that the flow is strongly three-dimensional, and that streamwise flow reversal and cross-stream secondary motion exist; similar flow phenomena have been experimentally observed. The strengths of the flow reversals and secondary motion are shown to increase with increasing Grashof number. The impact which these three-dimensional effects have on the friction factor, the Nusselt number, the buoyancy force, and the average axial velocity, are discussed.

INTRODUCTION

THIS PAPER concerns the steady-state, natural convection flow through a toroidal loop oriented in a vertical plane (see Fig. 1). When the loop is heated from below and cooled from above a density gradient is created in the fluid, and fluid motion results. If the loop is tilted through the angle α, as shown in the figure, the flow is in the counterclockwise direction.

This system is a simple example of a class of devices known as thermosyphons or natural circulation loops, which have applications in solar hot water heaters, emergency cooling of nuclear reactor cores, geothermal power production, computer cooling, etc. [1–7].

Two early analyses of natural circulation loops were performed by Welander [8] and by Keller [9]. Both were simplified, one-dimensional models which yielded steady-state and oscillatory solutions.

The thermosyphon configuration which is the subject of this study has been investigated previously. Creveling *et al.* [10] reported findings of an experimental investigation of this toroidal thermosyphon configuration with zero tilt angle (i.e. $\alpha = 0$ in Fig. 1). They found that a steady-state flow existed only for the high and low heat input ranges in their experiments. In the intermediate heat input range, the flow was unstable. Under steady-state conditions, they observed a region of flow reversal near the entrance to the cooling section. Creveling *et al.* also performed a steady-state, one-dimensional (θ-variation only) analysis of the fluid velocity and temperature. Damerell and Schoenhals [11] continued this work by investigating, both experimentally and analytically, the effect of tilting the thermosyphon about its horizontal axis ($\alpha \neq 0$ in Fig. 1). They found experimentally that the flow was always stable for a tilt angle greater than 6°.

Ramos *et al.* [12] addressed the effect of a variable cross-sectional area. The one-dimensional analysis was extended to the transient case in refs. [13, 14]. Mertol *et al.* [15, 16] performed a two-dimensional (r and θ) numerical analysis of the toroidal thermosyphon. Stern and Greif [17] undertook further experimental investigation of the same thermosyphon configuration. Three-dimensional effects were once again observed, such as flow reversal, nonzero cross-stream velocities, and nonaxisymmetric temperature profiles.

To summarize, experiments on the toroidal thermosyphon have shown that under stable flow conditions the flow is strongly three-dimensional, and regions of streamwise flow reversal exist. The one- and two-dimensional analyses performed to date have all assumed that the flow is solely in the axial direction and that the effect of pipe curvature is negligible. Because of these simplifications, these analyses have not been able to predict any of the three-dimensional flow phenomena. A three-dimensional analysis of this

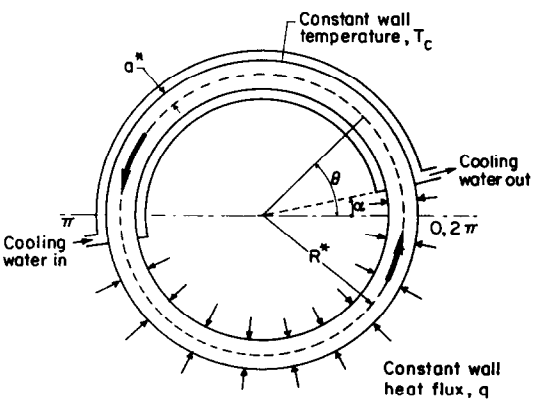

FIG. 1. The toroidal thermosyphon.

NOMENCLATURE

a^* radius of pipe
c specific heat
f friction factor
fRe friction factor times Reynolds number, $-\frac{4}{\bar{w}}\frac{\partial w}{\partial r}\Big|_1$
$\overline{fRe}$ peripherally averaged value of fRe, $\frac{1}{2\pi}\int_0^{2\pi} fRe(\phi,\theta)\,d\phi$
g gravitational constant
Gr Grashof number, $(g\beta\Delta T a^{*3})/\nu^2$
Gz Graetz number from ref. [15], $Re_{ch}Pra^*/\pi R^*$
h height above a datum
$\dot{m}$ characteristic mass flow rate, $\rho_c \pi a^{*2} W$
Nu Nusselt number, $\left(-2\frac{\partial\Phi}{\partial r}\Big|_1\right)\Big/(\Phi_w-\Phi_b)$
$\overline{Nu}$ peripherally averaged Nusselt number, $\left(2\int_0^{2\pi}\frac{\partial\Phi}{\partial r}\Big|_1 d\phi\right)\Big/\int_0^{2\pi}(\Phi_b-\Phi_w)\,d\phi$
p^* $\hat{p}+\rho_c gh$
$\hat{p}$ thermodynamic pressure
p nondimensional pressure, $p^*/\rho_c W^2$
Pr Prandtl number, ν/α
q_w nondimensional wall heat flux, $\frac{1}{2\pi}\int_0^{2\pi}\frac{\partial\Phi}{\partial r}\Big|_1 d\phi$
Q total heat input in heating section
r^*, r radial coordinate, $r = r^*/a$
R^*, R pipe radius of curvature, $R = R^*/a$
Re Reynolds number, $\rho_c w^* 2a^*/\mu$
Re_{ch} characteristic Reynolds number, $\rho_c W 2a^*/\mu$
T temperature
T_b bulk temperature, $\frac{1}{\bar{w}^*\pi a^{*2}}\int_0^{2\pi}\int_0^{a^*} w^* Tr^*\,dr^*\,d\phi$
T_c constant wall temperature in the cooling section
T_w wall temperature, $T(a^*,\phi,\theta)$
$\mathbf{u}$ nondimensional vector velocity
u^*, u radial velocity, $u = u^*/W$
v^*, v circumferential velocity, $v = v^*/W$
w^*, w axial velocity, $w = w^*/W$
$\bar{w}^*, \bar{w}$ cross-sectionally averaged axial velocity, $\bar{w} = \frac{1}{\pi}\int_0^{2\pi}\int_0^1 wr\,dr\,d\phi$
W characteristic axial velocity, $(g\beta Q/4\pi^3\mu c)^{1/2}$.

Greek symbols

α tilt angle, or thermal diffusivity
β coefficient of thermal expansion
ΔT characteristic bulk temperature difference, $Q/\dot{m}c$
θ axial coordinate
μ dynamic viscosity
ν kinematic viscosity, μ/α
ρ_c density evaluated at T_c
τ_w wall shear stress, $\frac{1}{2\pi}\int_0^{2\pi}\frac{\partial w}{\partial r}\Big|_1 d\phi$
Φ nondimensional temperature, $(T-T_c)/\Delta T$
Φ_b nondimensional bulk temperature, $(T_b-T_c)/\Delta T$
$\bar{\Phi}$ nondimensional average temperature, $\frac{1}{\pi}\int_0^{2\pi}\int_0^1 \Phi r\,dr\,d\phi$
Φ_w nondimensional wall temperature, $(T_w-T_c)/\Delta T$
ϕ circumferential coordinate.

flow has been carried out by Lavine [18]. Results showing the effect of tilt angle have been reported by Lavine *et al.* [19].

THEORETICAL BACKGROUND

A three-dimensional, numerical analysis of the flow and heat transfer in the toroidal thermosyphon has been performed. The flow is assumed to be steady-state, laminar and incompressible, and viscous dissipation is neglected. Physical properties are assumed to be constant, except that the Boussinesq approximation is used for the density. Given these assumptions, the nondimensional differential equations which govern the flow, expressed in the coordinate system shown in Fig. 2, are as follows (with symbols defined in the Nomenclature):

Continuity

$$\frac{1}{r}\frac{\partial}{\partial r}[r(R+r\cos\phi)u] + \frac{1}{r}\frac{\partial}{\partial\phi}[(R+r\cos\phi)v] + \frac{\partial w}{\partial\theta} = 0. \quad (1)$$

r-momentum

$$(\mathbf{u}\cdot\nabla)u - \frac{v^2}{r} - \frac{\cos\phi}{R+r\cos\phi}w^2 = -\frac{\partial p}{\partial r} + \frac{16\pi^4}{Gr}\Phi\sin\theta\cos\phi$$

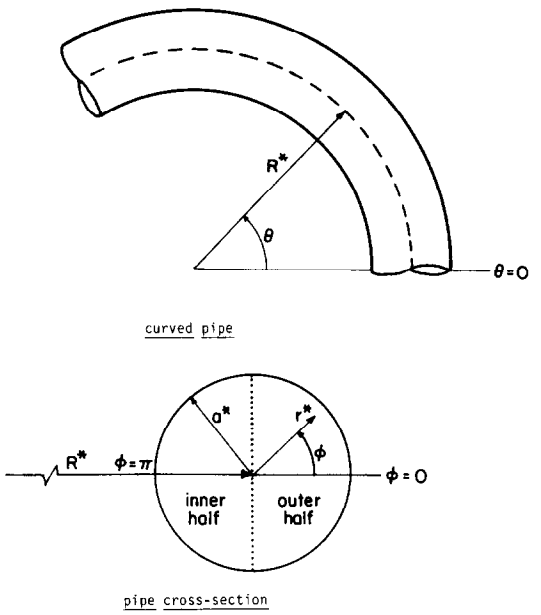

FIG. 2. The toroidal coordinate system.

$$+\frac{4\pi^2}{Gr}\left[\nabla^2 u-\frac{2}{r^2}\frac{\partial v}{\partial \phi}-\frac{u}{r^2}+\frac{\sin\phi}{r(R+r\cos\phi)}v+\frac{\cos\phi}{(R+r\cos\phi)^2}\left(v\sin\phi-u\cos\phi-2\frac{\partial w}{\partial\theta}\right)\right]. \quad (2)$$

ϕ-momentum

$$(\mathbf{u}\cdot\nabla)v+\frac{uv}{r}+\frac{\sin\phi}{R+r\cos\phi}w^2 = -\frac{1}{r}\frac{\partial p}{\partial\phi}-\frac{16\pi^4}{Gr}\Phi\sin\theta\sin\phi+\frac{4\pi^2}{Gr}\left[\nabla^2 v+\frac{2}{r^2}\frac{\partial u}{\partial\phi}-\frac{v}{r^2}-\frac{\sin\phi}{r(R+r\cos\phi)}u-\frac{\sin\phi}{(R+r\cos\phi)^2}\left(v\sin\phi-u\cos\phi-2\frac{\partial w}{\partial\theta}\right)\right]. \quad (3)$$

θ-momentum

$$(\mathbf{u}\cdot\nabla)w+\frac{w}{R+r\cos\phi}(u\cos\phi-v\sin\phi) = -\frac{1}{R+r\cos\phi}\frac{\partial p}{\partial\theta}+\frac{16\pi^4}{Gr}\Phi\cos\theta+\frac{4\pi^2}{Gr}\left[\nabla^2 w+\frac{2}{(R+r\cos\phi)^2}\times\left(\frac{\partial u}{\partial\theta}\cos\phi-\frac{\partial v}{\partial\theta}\sin\phi-\frac{w}{2}\right)\right]. \quad (4)$$

Energy

$$(\mathbf{u}\cdot\nabla)\Phi=\frac{4\pi^2}{PrGr}\nabla^2\Phi \quad (5)$$

where

$$(\mathbf{u}\cdot\nabla)=u\frac{\partial}{\partial r}+\frac{v}{r}\frac{\partial}{\partial\phi}+\frac{w}{R+r\cos\phi}\frac{\partial}{\partial\theta} \quad (6)$$

$$\nabla^2=\frac{1}{r(R+r\cos\phi)}\left[\frac{\partial}{\partial r}\left(r(R+r\cos\phi)\frac{\partial}{\partial r}\right)+\frac{1}{r}\frac{\partial}{\partial\phi}\left((R+r\cos\phi)\frac{\partial}{\partial\phi}\right)+\frac{1}{R+r\cos\phi}\frac{\partial}{\partial\theta}\left(r\frac{\partial}{\partial\theta}\right)\right]. \quad (7)$$

The boundary conditions are: (1) zero velocity at the wall; (2) specified wall temperature in the cooling section; (3) specified wall heat flux in the heating section; (4) finite velocities and temperature at the pipe centerline; (5) symmetry about the plane $\phi = 0, \pi$; and (6) 2π-periodicity in the θ direction. The solution to these equations depends on the four parameters Gr, Pr, R and α. Both the buoyancy and viscous terms are multiplied by $1/Gr$. This does *not* mean that buoyancy becomes less important as the Grashof number increases. Rather, since the characteristic velocity was derived based on a balance between buoyancy and friction, the nondimensional equations reflect this balance.

In the two-dimensional analysis of Mertol *et al.* [15], it was assumed that there is axial symmetry (i.e. no ϕ dependence), the velocity is solely in the axial direction, and pipe curvature and axial conduction are negligible.

The various one-dimensional analyses can be derived by integrating the three-dimensional axial momentum and energy equations over the pipe cross-section and then neglecting terms in the integrated equations. If it is assumed that the velocity is solely in the axial direction, and that pipe curvature and axial conduction are negligible, the integrated equations then reduce to [18]:

θ-momentum

$$\frac{1}{R}\frac{\mathrm{d}\overline{w^2}}{\mathrm{d}\theta}=-\frac{1}{R}\frac{\mathrm{d}\bar{p}}{\mathrm{d}\theta}+\frac{16\pi^4}{Gr}\bar{\Phi}\cos\theta+\frac{4\pi^2}{Gr}\frac{2\tau_w}{a}. \quad (8)$$

Energy

$$\frac{1}{R}\bar{w}\frac{\mathrm{d}\Phi_b}{\mathrm{d}\theta}=\frac{4\pi^2}{PrGr}\frac{2q_w}{a}. \quad (9)$$

In the one-dimensional analyses, the momentum equation is integrated around the loop from $\theta = 0$ to 2π so that the inertia and pressure gradient terms are eliminated. Thus, in the one-dimensional analyses the momentum equation reduces to an overall balance between buoyancy and friction. It is then assumed that Φ_b calculated from the energy equation is equal to $\bar{\Phi}$ needed in the momentum equation. This will be shown to be substantially in error in this paper.

To evaluate τ_w and q_w, the wall shear stress throughout the loop and the heat transfer coefficient in the cooling section must be specified in the one-

dimensional analyses. (The value of q_w in the heating section is a specified boundary condition.)

NUMERICAL SOLUTION

The differential equations (1)–(5) were solved using a finite-difference computer program. The computer program is a version of the TEACH code [20], a finite-difference program for solving the continuity, momentum and energy equations in their complete elliptic form. The concepts underlying this computer program are discussed by Patankar [21], and a version for curved pipes is described by Humphrey [22]. This computer program was modified for the toroidal thermosyphon flow by Lavine [18], and was validated on several flows for which experimental data or analytical solutions are available.

For the solution procedure used in this research, 'convergence' can have two meanings. For a particular finite-difference grid, the sequence of iterations must be continued until they converge to a reasonably accurate solution of the finite-difference equations. And, as the finite-difference grid is refined, the sequence of solutions must converge to a reasonably grid-independent result. When both of these criteria are met, the numerical solution will be a good approximation to a solution of the differential equations. Both of these criteria were met for the thermosyphon cases reported here [18], using a $39 \times 26 \times 100$ grid (in the r, ϕ and θ directions, respectively). The radial grid was nonuniform, with 13 of the 39 grids within a distance from the wall of 15% of the radius. The ϕ grid was uniform. The axial (θ) grid was nonuniform, with 8 of the 100 grids located in the first 10° of the cooling section, and another 8 in the first 10° of the heating section.

RESULTS

The solution for the flow depends on the four parameters Gr, Pr, R and α. The cases which are investigated in this study correspond to the geometry of the toroidal thermosyphons at Purdue University and at the University of California, Berkeley, i.e. $R = 24.6$. The Prandtl number is a typical value for water, $Pr = 6.5$. Unfortunately, it was not possible to obtain converged results for values of the Grashof number corresponding to the experimental data, which were on the order of 10^4. Cases are presented here for two lower Grashof numbers, $Gr = 1900$ and 3600, and a tilt angle of 10° (to ensure the existence of a steady-state flow). For $R = 24.6$, the values of Gr correspond to $Gz = 8$ and 15 in the two-dimensional analysis of Mertol *et al.* [15].

For the cases discussed here, the main flow is in the counterclockwise direction. However, regions of flow reversal do exist. Secondary motion (i.e. motion perpendicular to the axial or θ direction) was also predicted by the numerical analysis.

The results for the two different Grashof numbers are similar, and results for the higher Grashof number will only be shown when necessary to demonstrate a significant difference between the two cases. A larger Grashof number corresponds to steeper gradients of velocity and temperature, and also results in a stronger coupling between the temperature and velocity fields, which causes stronger flow reversals and secondary motion. The larger gradients at the wall and the higher secondary velocities yield greater wall friction and heat transfer. From the definitions of Gr and the characteristic Reynolds number (see Nomenclature), Gr is seen to be proportional to Re_{ch}.

Temperature and velocity profiles

For discussion purposes, the thermosyphon will be divided into four regions: the entrance to the cooling section, $\theta \approx 10$–$20°$, the remainder of the cooling section, $\theta \approx 20$–$190°$, the entrance to the heating section, $\theta \approx 190$–$200°$, and the remainder of the heating section, $\theta \approx 200$–$370°$.

Figures 3 and 4 show the dimensionless temperatures and axial velocity profiles in the symmetry plane, near the entrance to the cooling section, for $Gr = 1900$. The left- and right-hand sides of the graph correspond to the inner and outer pipe halves, respectively (see Fig. 2). Before the flow enters the cooling section ($\theta = 9.8°$), the temperature peak is at the inner wall (Fig. 3). This is because in the bottom half of the loop the hotter, lighter fluid rises toward the inner wall. The fluid enters the cooling section and the temperature at the wall drops to the specified wall temperature (see $\theta = 10.3°$). A steep temperature gradient exists near the wall, and the temperature in the core decreases as the flow proceeds downstream.

It is noted that the temperature peak shifts toward the outer wall since, as the pipe becomes more inclined, the hotter fluid tends to rise toward the outer wall, while the cold fluid in the neighborhood of the wall falls toward the inner wall. This creates a

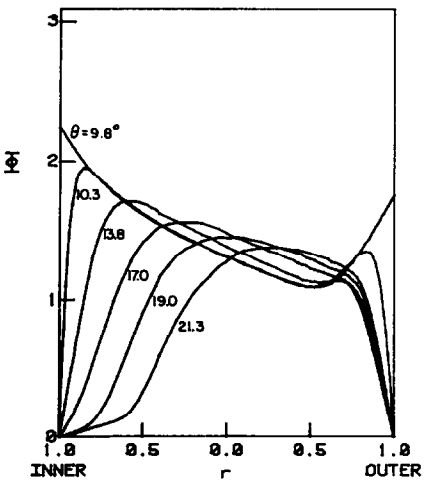

FIG. 3. Temperature profiles in symmetry plane, near cooling section entrance, $Gr = 1900$.

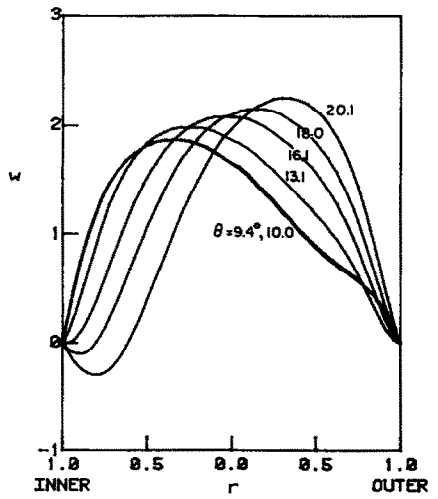

FIG. 4. Axial velocity profiles in symmetry plane, near cooling section entrance, $Gr = 1900$.

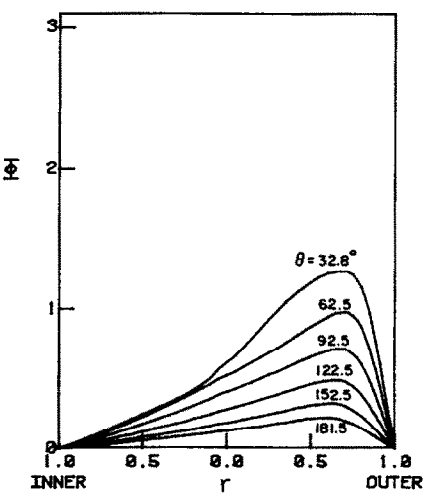

FIG. 6. Temperature profiles in symmetry plane, remainder of cooling section, $Gr = 1900$.

secondary motion, which becomes stronger as the flow proceeds downstream (see Fig. 5; the velocity vectors are shown at selected grid points to avoid cluttering the figure). The secondary velocity, $\sqrt{u^2+v^2}$, is as large as 50% of the average axial velocity at some points in the flow.

Next, consider the axial velocity profiles, Fig. 4. Before the flow enters the cooling section ($\theta = 9.4°$), the velocity peak is toward the inner wall, since the hotter fluid there rises more quickly than the cooler fluid at the outer wall. Once inside the cooling section ($\theta > 10°$), the flow begins to decelerate near the walls, due to the rapid cooling there. The cross-stream secondary motion brings the cold, slowly moving fluid in the neighborhood of the wall toward the inner wall (see Fig. 5). A flow reversal results at the inner wall, and the axial velocity peak shifts toward the outer wall. The temperature is considerably lower in the region of flow reversal than in the remainder of the cross-section (see Fig. 3).

For the higher Grashof number, $Gr = 3600$, the axial flow reversal begins earlier, becomes stronger and lasts longer, due to the increased importance of buoyancy. This stronger flow reversal forces the axial velocity peak to be closer to the outer wall.

The flow in the remainder of the cooling section is illustrated in Figs. 6 and 7 for $Gr = 1900$. The temperature decreases as the flow proceeds through the cooling section (Fig. 6). The temperature peak remains near the outer wall due to buoyancy effects. Next consider the axial velocity (Fig. 7). As the flow approaches the top of the loop ($\theta = 90°$), the component of the gravitational force in the axial direction goes to zero, so that there is no longer any reason for the cooler fluid to reverse its axial direction. Thus, the region of flow reversal gradually vanishes, and accordingly the magnitude of the axial velocity peak diminishes. After the flow passes the top of the loop, gravity causes the cooler fluid near the inner wall to fall more rapidly than the warmer fluid near the outer wall. Thus the velocity peak shifts toward the inner wall. This effect is small because the temperature variation across the cross-section is relatively small toward the end of the cooling section. For the higher Grashof number, the axial velocity peak moves somewhat closer to the inner wall due to a larger temperature variation and to the increased importance of buoyancy.

The general features of the flow in the heating section are similar to those in the cooling section; in the heating section the hotter fluid rises toward the inner wall, which results in a flow reversal near the

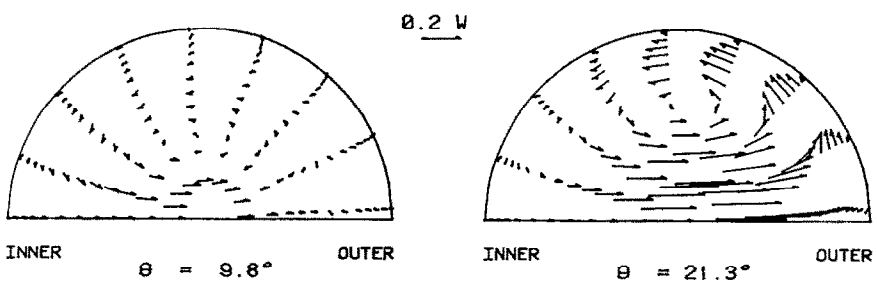

FIG. 5. Secondary velocity vectors near cooling section entrance, $Gr = 1900$.

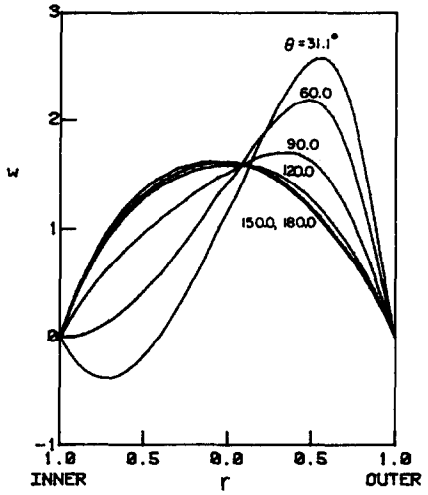

FIG. 7. Axial velocity profiles in symmetry plane, remainder of cooling section, $Gr = 1900$.

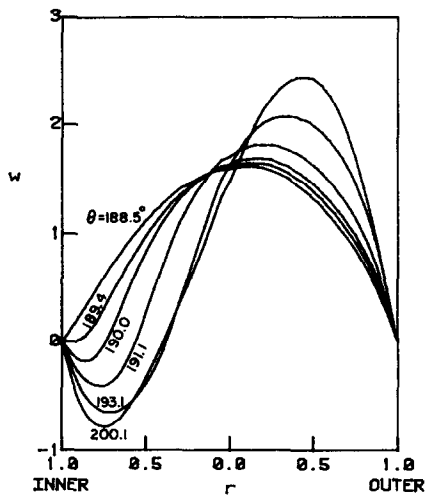

FIG. 9. Axial velocity profiles in symmetry plane, near heating section entrance, $Gr = 1900$.

beginning of the heating section. However, there are differences in the details of the flow in the two sections, due to the fact that the constant wall heat flux condition permits greater thermal stratification. To illustrate this, consider that at the top of the cooling section, the colder fluid falls toward the inner wall and the hotter fluid rises toward the outer wall. However, the fluid can never become hottest at the top, because the wall itself must be cold at the top. In contrast, at the bottom of the heating section, the colder fluid falls toward the outer wall and the hotter fluid rises toward the inner wall. Here the fluid may become strongly stratified, with the wall considerably hotter at the top (inner wall) than at the bottom (outer wall). The effects of this greater thermal stratification are discussed shortly.

Figures 8 and 9 are temperature and axial velocity profiles in the symmetry plane near the beginning of the heating section, for $Gr = 1900$. Note that the right sides of these (and all other) plots still correspond to the outer wall even though, if the thermosyphon is viewed as in Fig. 1, the outer wall is now to the left. The curves $\theta = 189.0°$ and $189.8°$ in Fig. 8 correspond to locations shortly upstream of the entrance to the heating section. The temperature curve for $\theta = 189.0°$ looks similar to the profile at $\theta = 181.5°$ in Fig. 6. However, at $\theta = 189.8°$, the temperature has risen significantly near the inner wall, even though the flow is still in the cooling section. This temperature increase is due to a region of axial flow reversal which causes fluid from the heating section to flow back into the cooling section. In the velocity profiles, Fig. 9, it is difficult to discern the small flow reversal at $\theta = 189.4°$, but at $\theta = 190.0°$ (exactly at the entrance to the heating section) it is quite apparent, and it becomes stronger as the flow proceeds. The speed of the reversed flow is greater in the heating section than in the cooling section (cf. Fig. 4). This is due to the greater thermal stratification in the heating section (see Fig. 8 which shows that the temperature is considerably hotter at the inner wall than at the outer wall), which causes a larger velocity variation over the cross-section (due to the effect of buoyancy). Thus, the flow reversal is stronger in the heating section and is able to penetrate into the cooling section.

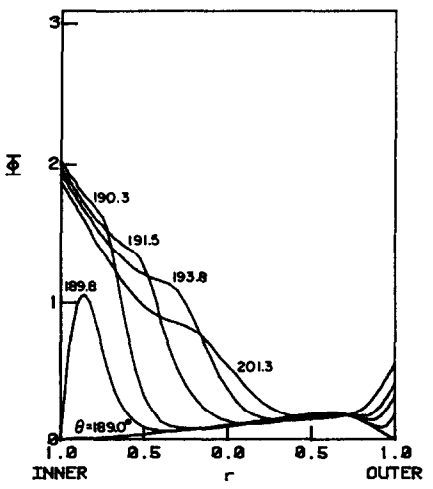

FIG. 8. Temperature profiles in symmetry plane, near heating section entrance, $Gr = 1900$.

The results for the higher Grashof number case near the entrance to the heating section are illustrated in Figs. 10 and 11 (cf. Figs. 8 and 9). It is seen that the flow reversal near the inner wall and the corresponding temperature peak start sooner and are more pronounced, due to the increased importance of buoyancy. In Fig. 11 the flow reversal does not begin *at* the inner wall, but rather a short distance away from the wall. Immediately adjacent to the wall the fluid continues to flow downward until it enters the heating section ($\theta = 190.0°$). The reason for this is that in the cooling section the region very close to the wall is quite cold. Since buoyancy (or gravity) is more important

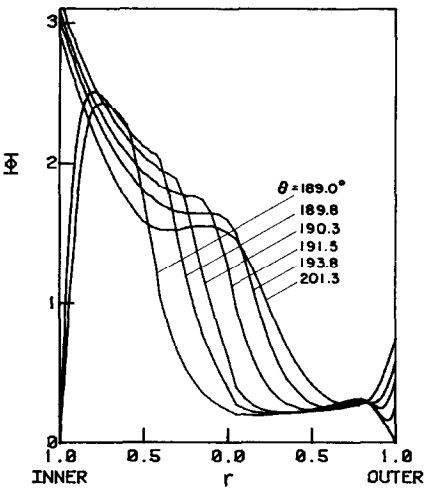

FIG. 10. Temperature profiles in symmetry plane, near heating section entrance, $Gr = 3600$.

for this case, this cold fluid has a stronger tendency to fall downward (in the main flow direction).

Next consider the secondary motion in the heating section. Throughout most of the heating section the hot fluid near the wall rises toward the inner wall, and the colder fluid falls toward the outer wall. Thus the secondary motion has the same pattern as in the cooling section—inward near the wall and outward near the symmetry plane. However, this characteristic secondary motion is weaker in the heating section because of the greater thermal stratification; that is, the fluid is more stably stratified (i.e. hotter near the top), and the driving force for the secondary motion is therefore weaker. There is another difference between the secondary motions in the two sections. Very near the entrance to the heating section there is a strong secondary motion which brings fluid from near the inner wall toward the outer wall over the entire pipe

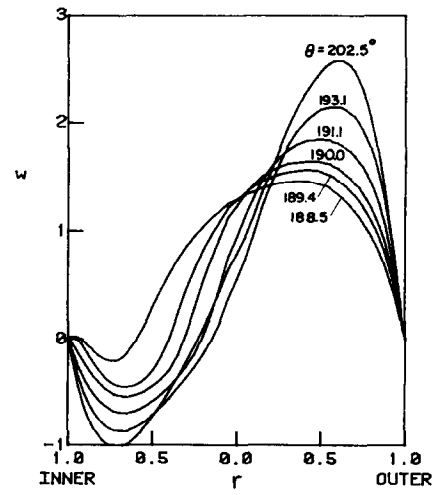

FIG. 11. Axial velocity profiles in symmetry plane, near heating section entrance, $Gr = 3600$.

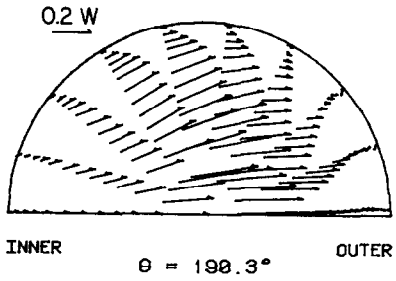

FIG. 12. Secondary velocity vectors near heating section entrance, $Gr = 1900$.

cross-section (see Fig. 12). This motion begins somewhat upstream of the flow reversal. The fluid moving in the main flow direction must move around the flow reversal, toward the outer wall. This effect is also present near the entrance to the cooling section, but is not as strong, because the flow reversal is weaker there, and because (as just explained) the driving force for the more characteristic secondary motion is stronger.

The temperature increases as the flow proceeds through the heating section (not shown). The temperature peak remains at the inner wall due to buoyancy effects. As the flow approaches the bottom of the loop the flow reversal vanishes and the axial velocity peak diminishes (not shown), similar to the behavior near the top of the cooling section. After the flow passes the bottom of the loop, buoyancy causes the warmer fluid near the inner wall to rise more quickly than the cooler fluid near the outer wall and the velocity peak therefore moves toward the inner wall. This effect is more pronounced in the heating section, because the temperature variation across a cross-section is greater for a constant wall heat flux boundary condition than for a constant wall temperature boundary condition.

For the higher Grashof number, the velocity peak moves slightly closer to the inner wall than it did for the lower Gr case, due to the larger temperature variation and to the increased importance of buoyancy.

Friction factors and Nusselt numbers

The results for the local value of fRe for the lower Grashof number case are shown in Fig. 13 as a function of ϕ for different values of θ. The coordinate ϕ varies from 180° to 0° so that the left- and right-hand sides of the graph correspond to the inner and outer walls, as before. In the flow reversal regions fRe is negative, since the velocity is in the opposite direction from the main flow (observe near the inner wall for $\theta = 31.1°$ and $211.1°$). The friction increases near the outer wall at these locations, since the axial velocity peak shifts toward the outer wall.

Figure 14 shows the peripherally averaged $\overline{fRe}$ (see Nomenclature). It is typically higher than for fully developed laminar flow in a straight pipe (i.e. 16), and is generally somewhat greater for the higher Gr case, as

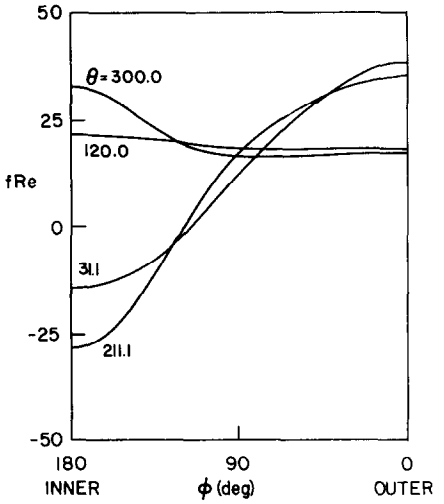

FIG. 13. Variation of fRe around tube periphery.

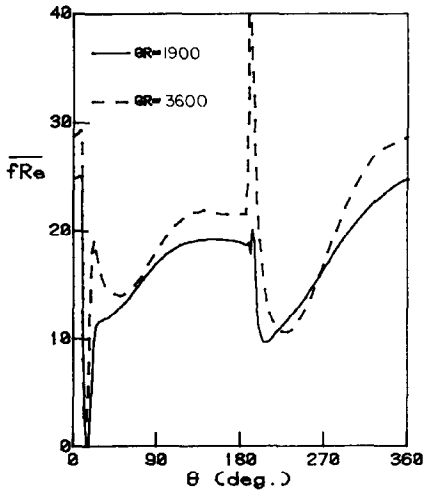

FIG. 14. Peripherally averaged fRe as a function of θ.

expected. The variation of $\overline{fRe}$ with θ is quite complicated. In portions of the flow reversal regions $\overline{fRe}$ drops significantly due to the 'negative' friction at the inner wall. However, the flow reversals also shift the axial velocity peak toward the outer wall, causing increased friction there. For the higher Gr case, this effect dominates at approximately $\theta = 30°$ and 190°, causing large peaks at these two locations. A comparison of Figs. 9 and 11 at $\theta = 190°$ confirms that the axial velocity gradient at the outer wall is significantly greater for the higher Gr case. Apparently, flow reversals may either decrease or increase the value of $\overline{fRe}$ at a particular cross-sectional location, depending on the local details of the flow. The value of fRe when averaged over the entire loop (i.e. in *both* the peripheral and axial directions) is 16.8 for $Gr = 1900$, and 19.5 for $Gr = 3600$.

In Fig. 15, the local Nusselt number is seen to vary strongly around the tube periphery. The peripherally

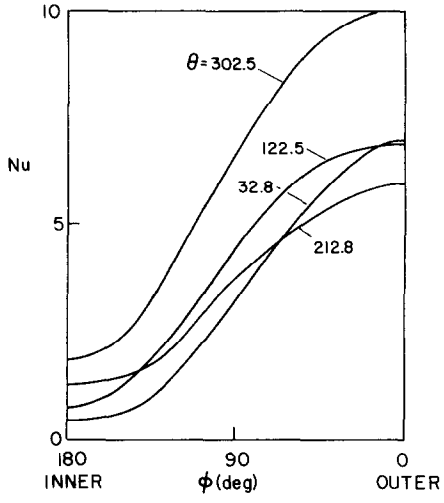

FIG. 15. Variation of Nu around tube periphery.

averaged Nusselt number, $\overline{Nu}$ (see Nomenclature), is shown in Fig. 16. At the entrances to both the cooling and heating sections, the Nusselt number drops sharply in a manner that is characteristic of the development of a thermal boundary layer. However, the Nusselt number does not continue to decrease monotonically as had been predicted by the two-dimensional analysis of Mertol *et al.* [15], indicating that three-dimensional effects are indeed important. $\overline{Nu}$ is generally higher for the higher Gr case, as anticipated.

Average velocities and temperatures

The average dimensionless axial velocities are 0.824 and 0.678 for the lower and higher Grashof numbers, respectively. (Note, however, that this does not necessarily mean that the *dimensional* velocity is lower for the higher Grashof number.) The dimensionless bulk temperature, Φ_b, is shown in Fig. 17. An energy

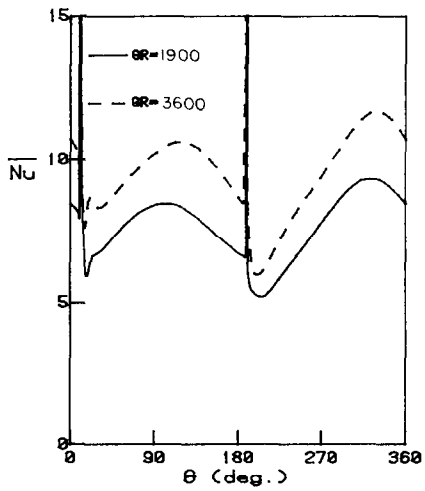

FIG. 16. Peripherally averaged Nu as a function of θ.

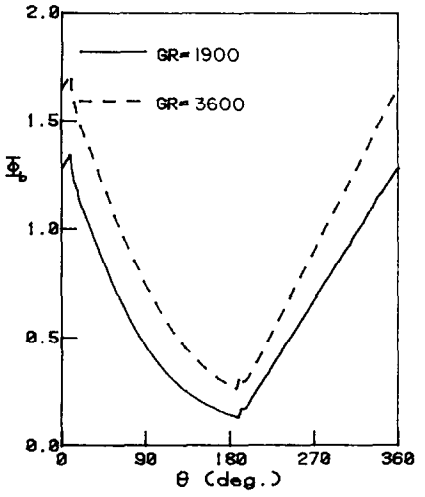

FIG. 17. Bulk temperature as a function of θ.

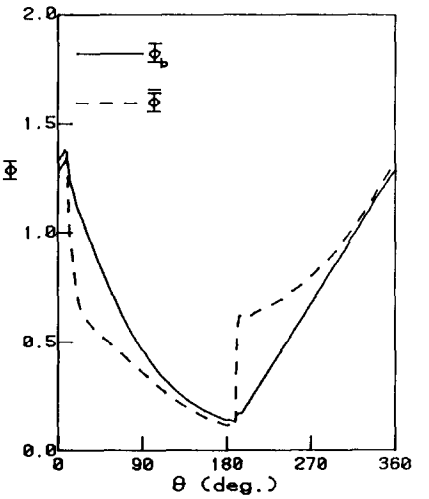

FIG. 18. Bulk and average temperatures, $Gr = 1900$.

balance on the heating section requires that $\Phi_b(\alpha) - \Phi_b(\pi+\alpha) = 1/\bar{w}$. It can be confirmed that the temperature differences shown on the graph are indeed inversely proportional to the average velocities given above. The rate of decrease of the bulk temperature in the cooling section is greatest at the entrance and then decays, consistent with constant wall temperature cooling. Since the flow at the higher Grashof number develops more slowly, the bulk temperature of the fluid in the cooling section approaches the cold wall temperature more slowly than for the lower Grashof number case. The increase of the bulk temperature in the heating section is essentially linear throughout most of the heating section. This is a consequence of the constant wall heat flux boundary condition, provided that axial conduction is negligible. Note, however, that at the entrance to the heating section the temperature increase is not linear; it increases and then actually decreases. Since the axial velocity varies from positive to negative over the cross-section, there is a region where the axial velocity is small, and hence axial conduction is locally significant compared to axial convection. This may give rise to the nonlinear bulk temperature profile.

The cross-sectionally averaged buoyancy force (discussed below) is proportional to the cross-sectionally averaged temperature, $\bar{\Phi}$. The bulk temperature, Φ_b, is a *velocity*-weighted average. These two types of average temperature are compared in Figs. 18 and 19 for the two cases. Near the entrance to the cooling section, high temperature regions correspond to high velocity regions, so the velocity weighted bulk temperature is greater than the average temperature. Near the entrance to the heating section, high temperature regions correspond to low (or even negative) velocity regions, so the velocity weighted bulk temperature is lower than the average temperature. The deviation of the average temperature from the bulk temperature is much greater for the higher Gr case. This is a consequence of the greater variation in the velocity and temperature profiles over a cross-section.

A discussion of the average axial velocity

The axial momentum equation, when averaged over the entire volume of the thermosyphon, reduces (to a very close approximation [18]) to a balance between the 'total buoyancy' and 'total wall friction'. It can then be shown [18] that:

$$\bar{w} = \frac{\frac{\pi}{4}\int_0^{2\pi} \bar{\Phi}\cos\theta\,\mathrm{d}\theta}{\frac{1}{2\pi}\int_0^{2\pi} \frac{\overline{fRe}}{16}\,\mathrm{d}\theta} = \frac{\text{total buoyancy}}{\text{total wall friction}}. \quad (10)$$

(This can also be derived by integrating equation (8) from $\theta = 0$ to 2π.) Table 1 lists the quantities $(\pi/4)\int_0^{2\pi} \bar{\Phi}\cos\theta\,\mathrm{d}\theta$, $(1/2\pi)\int_0^{2\pi} (\overline{fRe}/16)\,\mathrm{d}\theta$ and $\bar{w}$ for the one-, two- and three-dimensional analyses, for the two cases considered here. The two-dimensional

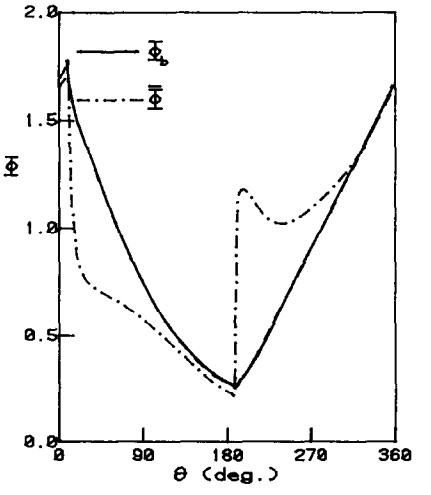

FIG. 19. Bulk and average temperatures, $Gr = 3600$.

Table 1. Comparison of one-, two- and three-dimensional analyses

	3-D		2-D		1-D	
Gr	1900	3600	1900	3600	1900	3600
$\frac{1}{2\pi}\int_0^{2\pi}\overline{(fRe/16)}\,d\theta$	1.05	1.22	1.05	1.21	1.00	1.00
$\frac{\pi}{4}\int_0^{2\pi}\bar{\Phi}\cos\theta\,d\theta$	0.87	0.83	0.97	1.08	1.00	1.00
$\bar{w}$	0.82	0.68	0.92	0.89	1.00	1.00
% error in $\bar{w}$ relative to three-dimensional results	—	—	12%	31%	21%	47%

results are from Mertol *et al.* [15], for the case of zero tilt angle. The one-dimensional results are derived using the analysis of Greif *et al.* [13], with the inclusion of a variable tilt angle. For the one-dimensional analysis, it is assumed that $\overline{fRe} = 16$ and $Nu = 3.658$ in the cooling section.

First let us consider the three-dimensional results. As described previously, the friction is greater for the higher Grashof number case. In addition, the total buoyancy is less for the higher Grashof number than for the lower Grashof number. This is due to the stronger flow reversals for the higher Grashof number, which cause the average temperature to decrease more quickly near the cooling section entrance (where the flow is rising) and increase more quickly near the heating section entrance (where the flow is falling) (cf. Figs. 18 and 19). Both of these temperature effects act to retard the flow, or decrease the total buoyancy. The combined effects of higher friction and lower buoyancy cause the average axial velocity to be lower for the higher Grashof number case.

The one-dimensional analysis assumed a value of 16 for $\overline{fRe}$, which in general is low. The one-dimensional analysis also overpredicts the total buoyancy, due, in part, to the incorrect assumption that the bulk temperature is equal to the average temperature. The three-dimensional analysis shows that, as compared to the bulk temperature, the average temperature drops more rapidly near the cooling section entrance and rises more quickly near the heating section entrance. As explained earlier, this tends to reduce the total buoyancy. Thus, the one-dimensional analysis, which neglects this effect, overpredicts the total buoyancy for these cases.

The two-dimensional analysis yields an excellent estimate of the total frictional force for the two cases given (assuming that the results for $\alpha = 0°$ would be approximately the same as for $\alpha = 10°$). The predicted total buoyancy, however, is significantly in error. This is due to the neglect of three-dimensional effects and the consequent inability to predict the flow reversals. In the absence of flow reversal, the bulk and average temperatures would probably differ much less. Thus, while the two-dimensional analysis does *not* make the assumption that the bulk and average temperatures are equal, the result is much the same as if it did. Therefore, as in the one-dimensional analysis, the two-dimensional analysis overpredicts the total buoyancy for the two cases.

Since both the one- and two-dimensional analyses overpredict the total buoyancy (and the one-dimensional analysis also underpredicts the friction), both analyses overpredict the average axial velocity.

CONCLUSIONS

Detailed numerical results for the flow in the thermosyphon are presented for two different Grashof numbers. The calculated results for these Grashof numbers do exhibit the flow phenomena which have been experimentally observed at higher Grashof numbers, such as axial flow reversal and cross-stream secondary motion.

The details of the flow, in particular the flow reversals and the secondary motion, depend on the Grashof number and on the thermal boundary condition (i.e. constant wall temperature or constant wall heat flux). The strength of the secondary motion and of the flow reversals is greater for the higher Grashof number case.

The calculated velocities and temperatures vary in all three dimensions, and the derived quantities $fRe(\phi,\theta)$ and $Nu(\phi,\theta)$ are strongly dependent on both ϕ and θ. The peripherally averaged quantities $\overline{fRe}$ and $\overline{Nu}$ are generally greater than for fully developed laminar flow in a straight pipe, except that $\overline{fRe}$ decreases strongly in the flow reversal regions. Both of these quantities are higher for the higher Grashof number case.

The cross-sectionally averaged (non-velocity-weighted) temperature may differ significantly from the bulk temperature. This is especially true in regions of strong flow reversal, since the axial velocity takes on extreme positive and negative values. The difference between the average and bulk temperatures is more pronounced for the higher Grashof number case, corresponding to the stronger flow reversals for this condition.

The total buoyancy decreases with increasing Grashof number. This is due to the stronger flow reversals at the higher Grashof number, which cause the average temperature, $\bar{\Phi}$, to decrease more strongly near the cooling section entrance, and increase more strongly near the heating section entrance.

The nondimensional average axial velocity is proportional to the ratio of the total buoyancy to the total friction, and is therefore lower for the higher Gr case, corresponding to lower total buoyancy and higher total friction.

The one- and two-dimensional analyses overpredict the total buoyancy, and consequently overpredict the average velocity.

Acknowledgements—The authors gratefully acknowledge the support received from the National Science Foundation and from IBM.

REFERENCES

1. D. Japikse, Advances in thermosyphon technology. In *Advances in Heat Transfer* (Edited by T. F. Irvine, Jr. and J. P. Hartnett), Vol. 9, pp. 1–111. Academic Press, New York (1973).
2. S. Ostrach, Natural convection in enclosures. In *Advances in Heat Transfer* (Edited by T. F. Irvine, Jr. and J. P. Hartnett), Vol. 8, pp. 161–227. Academic Press, New York (1972).
3. H. R. McKee, Thermosiphon reboilers—a review, *Ind. Engng Chem.* **62**, 76–82 (1970).
4. Y. Zvirin, A review of natural circulation loops in pressurized water reactors and other systems, *Nucl. Engng Des.* **67**, 203–225 (1981).
5. A. Mertol, W. Place, T. Webster and R. Greif, Detailed loop model (DLM) analysis of liquid solar thermosyphons with heat exchangers, *Sol. Energy* **27**, 367–386 (1981).
6. B. Norton and S. D. Probert, Natural-circulation solar-energy stimulated systems for heating water, *Appl. Energy* **11**, 167–196 (1982).
7. A. Mertol and R. Greif, A review of natural circulation loops. In *Natural Convection: Fundamentals and Applications* (Edited by W. Aung, S. Kakac and R. Viskanta). Hemisphere, New York (1985).
8. P. Welander, On the oscillatory instability of a differentially heated fluid loop, *J. Fluid Mech.* **29**, 17–30 (1967).
9. J. B. Keller, Periodic oscillations in a model of thermal convection, *J. Fluid Mech.* **26**, 599–606 (1966).
10. H. F. Creveling, J. F. De Paz, J. Y. Baladi and R. J. Schoenhals, Stability characteristics of a single-phase free convection loop, *J. Fluid Mech.* **67**, 65–84 (1975).
11. P. S. Damerell and R. J. Schoenhals, Flow in a toroidal thermosyphon with angular displacement of heated and cooled sections, *J. Heat Transfer* **101**, 672–676 (1979).
12. E. Ramos, M. Sen and C. Treviño, A steady-state analysis for variable area one- and two-phase thermosyphon loops, *Int. J. Heat Mass Transfer* **28**, 1711–1719 (1985).
13. R. Greif, Y. Zvirin and A. Mertol, The transient and stability behavior of a natural convection loop, *J. Heat Transfer* **101**, 684–688 (1979).
14. A. Mertol, A. Lavine and R. Greif, A study of the variation of the pressure in a natural circulation loop, *Int. J. Heat Mass Transfer* **27**, 626–630 (1984).
15. A. Mertol, R. Greif and Y. Zvirin, Two-dimensional study of heat transfer and fluid flow in a natural convection loop, *J. Heat Transfer* **104**, 508–514 (1982).
16. A. Mertol, R. Greif and Y. Zvirin, Two dimensional analysis of transient flow and heat transfer in a natural circulation loop, *Warme- u. Stoffubertr.* **18**, 89–98 (1984).
17. C. Stern and R. Greif, Measurements in a natural convection loop, submitted for publication.
18. A. G. Lavine, A three-dimensional analysis of natural convection in a toroidal loop. Ph.D. thesis, University of California, Berkeley (1984).
19. A. S. Lavine, R. Greif and J. A. C. Humphrey, A three-dimensional analysis of natural convection in a toroidal loop—the effect of tilt angle, *J. Heat Transfer* (in press).
20. A. D. Gosman and F. J. K. Ideriah, TEACH-2E: A general computer program for two-dimensional, turbulent, recirculating flows, Imperial College, London. Available as University of California, Berkeley, Department of Mechanical Engineering Report No. FM-83-2 (1983).
21. S. V. Patankar, *Numerical Heat Transfer and Fluid Flow*, 1st edn. McGraw-Hill, New York (1980).
22. J. A. C. Humphrey, Numerical calculations of developing laminar flow in pipes of arbitrary curvature radius, *Can. J. chem. Engng* **56**, 151–164 (1978).

ANALYSE TRIDIMENSIONNELLE DE LA CONVECTION NATURELLE DANS UNE BOUCLE TOROIDALE—EFFET DU NOMBRE DE GRASHOF

Résumé—On conduit une analyse numérique tridimensionnelle de la convection naturelle dans une boucle fermée toroïdale. Les résultats montrent que l'écoulement est fortement tridimensionnel et qu'il existe un écoulement de retour et un écoulement secondaire transversal; des phénomènes d'écoulements similaires ont été observés expérimentalement. Les intensités des retours et des mouvements transverses augmentent avec le nombre de Grashof. On discute de l'impact que ces effets ont sur le frottement, le nombre de Nusselt, les forces de volume et la vitesse moyenne axiale.

EINE DREIDIMENSIONALE ANALYSE DER NATÜRLICHEN KONVEKTION IN EINEM TORUS—EINFLUSS DER GRASHOF-ZAHL

Zusammenfassung—Eine dreidimensionale numerische Analyse der natürlichen Konvektion in einem Torus wurde durchgeführt. Die Ergebnisse zeigen, daß die Strömung einen ausgeprägten dreidimensionalen Charakter besitzt, und daß Rückströmung und Sekundärbewegung in Form einer Querströmung vorhanden sind; ähnliche Strömungsphänomene sind experimentell beobachtet worden. Es zeigt sich, daß die Stärke der Rückströmung und der Sekundärbewegung mit wachsender Grashof-Zahl zunimmt. Der Einfluß, welchen diese dreidimensionalen Effekte auf den Reibungsbeiwert, die Nusselt-Zahl, die Auftriebskraft und die mittlere axiale Geschwindigkeit ausüben, wird erörtert.

АНАЛИЗ ПРОСТРАНСТВЕННОЙ ЕСТЕСТВЕННОЙ КОНВЕКЦИИ В ТОРОИДАЛЬНОМ КОНТУРЕ. ЗАВИСИМОСТЬ ОТ ЧИСЛА ГРАСГОФА

Аннотация—Представлен численный анализ трехмерной естественной конвекции в замкнутом тороидальном контуре. Результаты показывают, что поток является полностью трехмерным и что имеет место его реверсирование и вторичное течение в поперечном направлении. Такие течения наблюдались в эксперименте. Показано, что интенсивности обратного и вторичного течений возрастают с увеличением числа Грасгофа. Рассматривается влияние этих пространственных эффектов на коэффициент трения, число Нуссельта, подъемную силу и среднюю по оси скорость течения.